ELSEVIER

Chemical Engineering Journal 77 (2000) 93–98

Chemical Engineering Journal

www.elsevier.com/locate/cej

Measurements of gas–liquid mixing in a stirred vessel using electrical resistance tomography (ERT)

M. Wang *, A. Dorward, D. Vlaev, R. Mann

Virtual Centre for Industrial Process Tomography, Department of Chemical Engineering, UMIST, Manchester, M60 1QD, UK

Abstract

The non-invasive measurement of mixing inside a stirred vessel in 3-D, using an 8×16 array of resistance tomography sensors, provides powerful opportunities for characterising and quantifying the process complexities [R. Mann, F.J. Dickin, M. Wang, T. Dyakowski, R.A. Forrest, P.J. Holden, Chem. Eng. Sci. 52 (1997) 2087–2097; P.J. Holden, M. Wang, R. Mann, F.J. Dickin, R.B. Edwards, A.I.Ch.E. JI. 44 (1998) 780–790]. Using the UMIST pilot plant 1.5 m stirred vessel, new results are presented for gas–liquid mixing which can distinguish differences in liquid mixing behavior between water (low viscosity) and relatively viscous 0.05% carbopol solution. The slower liquid phase tracer mixing rates for the viscous case compared with water, as well as differences in the pattern of mixing, can be readily observed and portrayed in 3-D using linear back projection for the reconstruction. In addition, the variation of local gas hold-up (voidage) can also be simultaneously measured by identifying regions within the vessel which have high or low local conductivity/resistivity. Electrical resistance tomography (ERT) can thus provide simultaneous detailed information on two aspects of gas–liquid mixing, involving the isolation of liquid phase mixing when gas–liquid mixing is taking place. The ERT results can be processed to provide the local mixing curve, hence mixing times, for any nominated pixel.

Keywords: Gas–liquid mixing; Stirred vessel; Tomography

1. Introduction

Fluid mixing processes are widely encountered in the chemical industries and stirred vessels are often used for such mixing duties. Unfortunately, these commonly encountered mechanical configurations for achieving mixing rarely have any instrumentation for monitoring or measuring the mixing per se. This means that in industrial practice, the specification and design of mixing vessels is based on empiricisms and rules of thumb. Conversely, the usually turbulent fluid mechanics in stirred vessels pose difficult unresolved computational and theoretical modelling difficulties.

Attempts are being made to pursue the science and fundamentals of mixing using advanced computational fluid dynamics (CFD) codes [3,4]. However, the resolution of the complex uncertainties in this modelling approach is inhibited by a relative lack of sufficiently detailed measurements for temporal and especially spatial validation and corroboration.

However, process tomography presents some interesting new opportunities for both validating CFD and for advancing understanding of mixing fundamentals. The most important aspect of this is the provision of a requisite density of information in the interrogated process space, coupled with a fast measurement acquisition. The essential non-invasiveness of electrical techniques is also important because the mixing in 3-D is not disturbed by the measurement process. The feasibility of electrical resistance tomography (ERT) to measure mixing was first established at a laboratory scale [5] and subsequently at full plant scale [1]. The suitability of a simplified modelling based on networks-of-zones was also established [6]. For homogeneous single phase miscible liquid mixing, the use of stacks of tomograms and solid-body 3-D representations has been shown to be capable of distinguishing the mixing produced by different impeller types [2]. The detailed level of information provided by tomographic techniques will be a powerful adjunct to recent developments applying CFD to complex gas–liquid reactors [7]. Electrical tomography has also been shown to be useful in detecting so-called 'pathological' mixing conditions inside a stirred vessel caused by equipment malfunction [8]. The potential for resistance tomography applications to chemical processes is not confined to mixing, as recent examples of separations in a cyclone [9] and for solid–fluid filtration [10] have demonstrated.

* Corresponding author.

1385-8947/00/$ – see front matter
PII: S1385-8947(99)00138-2

The two-phase mixing of gas and liquid in stirred vessels provides even greater complexity than the single phase case. Such gas–liquid mixing is, however, crucial to the manufacture of a range of key chemical intermediates. Typically gases such as hydrogen, chlorine, oxygen, etc., are contacted with hydrocarbon liquids. Also the mixing of air in stirred bioreactors is important because of the sensitivity of micro-organisms to dissolved oxygen levels. This paper outlines some new illustrative results for gas–liquid mixing in UMIST's 1.5 m diameter stirred vessel. It will be shown that ERT can discriminate the differences in pattern of pseudo-stationary gas hold-up in 3-D caused by variations in liquid phase viscosity. Moreover, the important dynamics of the mixing in the fluid phase can be simultaneously measured by following the conductivity changes in space and time following the injection of a pulse of high conductivity fluid tracer.

2. ERT system for 2.3 m^3 stirred vessel

Fig. 1 shows an interior view of UMIST's 1.5 m stirred vessel equipped with 8-planes of 16-sensor rings. The vessel is shown fitted with a Rushton turbine impeller (one-third of the vessel diameter) in a standard configuration with four equispaced wall-mounted baffles. This configuration was used for all the results reported here. Water (low viscosity) or carbopol solution (high $\approx$ 100 cP viscosity) was filled to a depth equal to the vessel diameter, so that the fluid volume was 2.3 m^3.

Air was fed into the vessel along a pipe fixed close to a baffle which was led across the floor and injected upwards directly below the center of the disc turbine. This gas feed pipe can be seen in Fig. 1. Several rings of sensors are also visible in Fig. 1. Full details have been given previously [1].

The results to be presented were obtained using an adjacent pairs protocol at 9.6 kHz. Tomogram sections were reconstructed by linear back projection from an initial zeroed datum which represented the fluid electrical conductivity and eliminated the effects of the stirrer and baffle fitments. The 3-D solid body realisations were smoothed by interpolation between the 8 planes using 'Spyglass' graphics.

3. Pseudo-stationary gas–liquid mixing

Fig. 2a, b and c present some illustrative results showing the potential of ERT to distinguish different patterns of gas–liquid mixing as indicated by the locally varying gas voidage distribution. When a liquid is stirred and gas is injected below the impeller the rotation of the stirrer breaks-up the entering gas stream into bubbles which are directed (in this case) radially outward by the impeller action. The bubbles generated rise by buoyancy and respond to the pattern of liquid flow also created by the impeller. The size of the bubbles, their rise velocity and their vector velocity (determined by local liquid direction and velocity) together govern the resultant 'instantaneous' pseudo-stationary pattern of local voidage/gas hold-up of dispersed bubbles. Because the local resistivity is reduced by the void spaces in the fluid occupied by bubbles, the map of resistivity sensed in 3-D reflects the spatial distribution, hence mixing of the gas throughout the fluid. The local voidage and the consequent local gas–liquid surface area are important in determining the absorption rate of any soluble component in the gas. This mass transfer flux can interact with chemical reactions to alter the chemical selectivity for complex reactions (these are often present in hydrocarbon fluids). Hence quantifying the gas–liquid mixing is important in accounting for observed chemical yields.

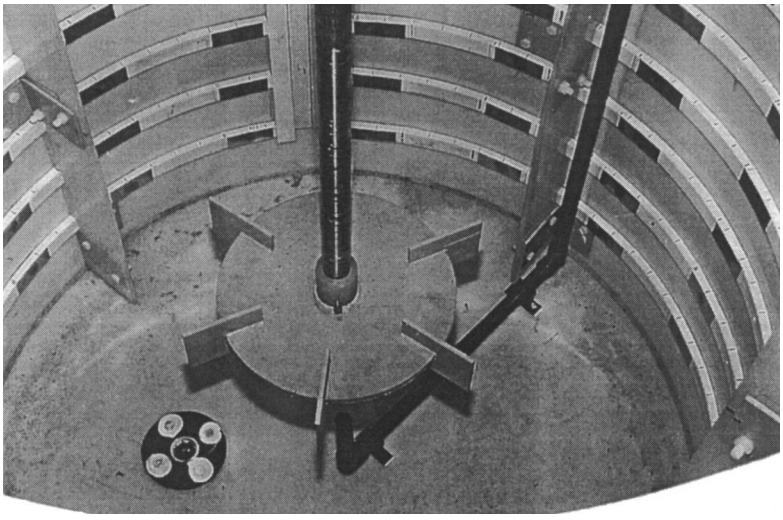

Fig. 1. Retro-fitted tomography system on 1.5 m stirred vessel.

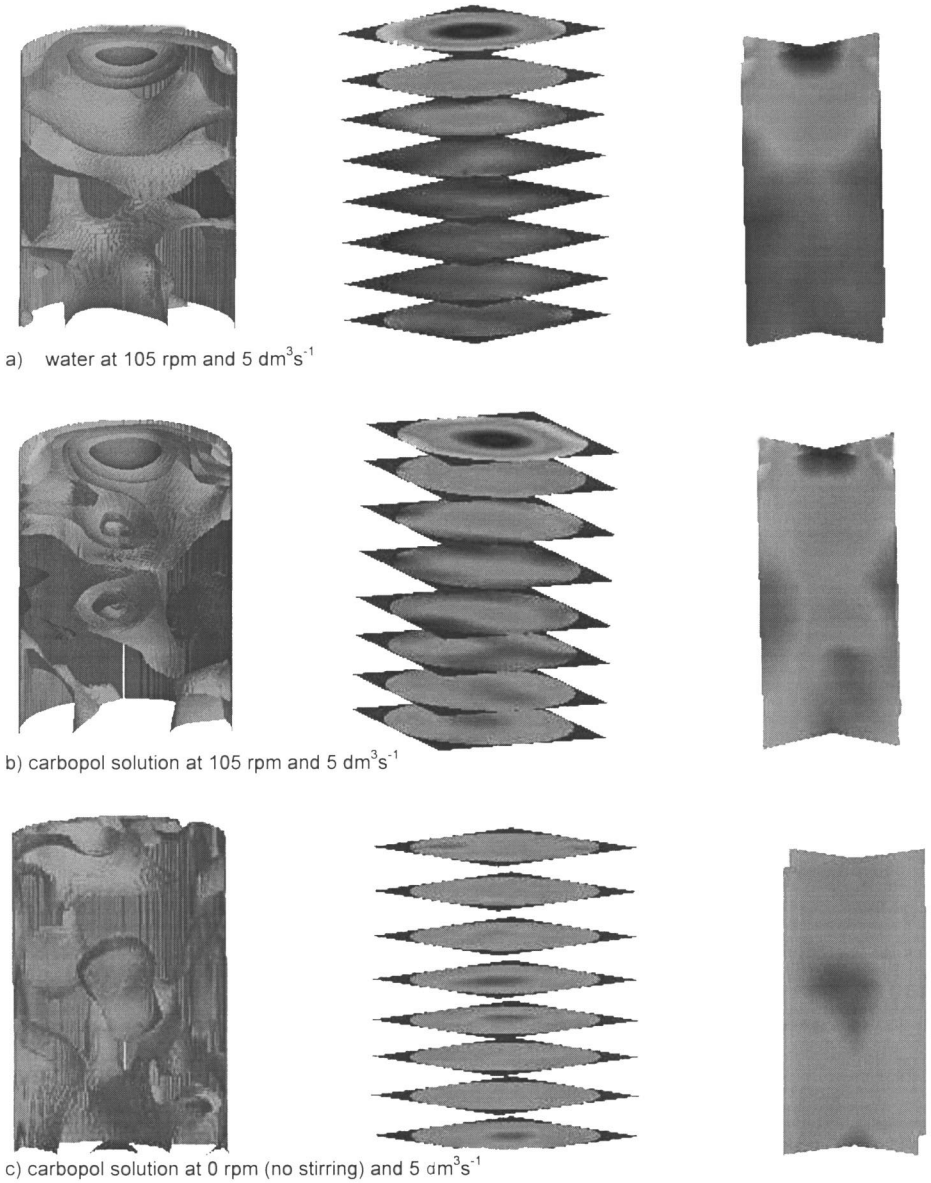

Fig. 2. Tomography of gas–liquid mixing.

3.1. Air–water low viscosity mixing

Fig. 2a shows results for air–water (low viscosity) at a stirrer speed of 73 rpm and a gas feed rate of $5\,dm^3\,s^{-1}$. The left-hand image shows a solid-body representation for the state of gas–liquid mixing. A region of high gas hold-up shows as an hour-glass shape, pinched at the middle. Across the top of the vessel there is an annular region of lower gas hold-up (darker) within the centre of which (coinciding with the central axis of the vessel) is a region of higher gas hold-up. This spatial pattern portrayed as solid-body contours is a unique measure of the gas–liquid mixing behaviour. The central part of Fig. 2a shows the same results in the format of a vertical stack of eight tomograms, one for each sensing plane. The right hand part shows yet another possible format with two vertical interesecting orthogonal planes.

3.2. Air–carbopol high viscosity mixing

The comparison with gas injected into a much more viscous fluid (0.05% carbopol in water, viscosity $\approx$ 100 cP) is then depicted in Fig. 2b. Differences in gas dispersion behaviour can be immediately seen by comparing the two left-hand solid-body images. A region of higher gas hold-up now spreads more widely throughout the vessel, although the pinched hour-glass shape is still present in the vicinity of the impeller (which is at half the vessel height). Fig. 2b confirms that the higher viscosity fluid (typical of manufacturing biorectors) creates a higher hold-up overall. This

probably reflects the fact that bubbles rise more slowly in a viscous fluid and coalesce less than in water. Both these factors would act to increase the overall hold-up of gas created by the impeller at the same gas flow rate and stirrer speed.

3.3. Gas–liquid mixing with and without stirring

That the stirring creates better gas–liquid mixing and produces a higher gas hold-up can be seen from Fig. 2c. This shows the result when, for the viscous carbopol solution, the stirrer is switched off, but with the same gas flow of $5\,dm^3\,s^{-1}$. The levels of local hold-up are now quite different and much lower overall, with a distinct low hold-up now showing above the impeller disc. This seems to reflect the fact that without stirring, the injected gas is deflected around the Rushton turbine disc and rises upwards closer to the walls. In the absence of any fluid circulation, the pattern of gas hold-up is markedly different. It remains a challenge to link these results to gas–liquid bubbly-flow modelling using spatially distributed models like networks-of-zones [6].

4. Dynamic unsteady mixing of the liquid phase

If the local gas hold-up induced variable resistivity of each reconstructed plane is zeroed to a new datum, the dynamic liquid phase mixing can be followed in space and time following the sudden injection of a high conductivity tracer pulse. This technique was previously used to follow single phase liquid mixing when no gas injection was taking place [1,2]. Exactly the same technique was used here for the injection of $1\,dm^3$ of saturated brine solution. The results are depicted in Fig. 3a and b for the same stirrer speed (73 rpm) and gas flow ($5\,dm^3\,s^{-1}$) as in Fig. 2.

4.1. Mixing represented by stacks of tomograms

Although the resistivity results are from different base lines due to the higher conductivity of the corbopol solution, the changes in resistivity cover approximately the same range as mixing takes place. This is to be expected since the pulse of brine tracer is identical in each case and the backgrounds are of low conductivity. As a result, the differences in liquid phase mixing can be immediately recognised when sets of images are compared side-by-side as in Fig. 3. The carbopol–air results are in Fig. 3a for times of 0, 3.75, 7.5, etc., with the water results in Fig. 3b. In comparing these two figures, from which the gas–liquid mixing effect has been isolated, it is immediately clear from the second ‘frame’ at 3.75 s that the rate of liquid phase mixing is much higher for the less viscous water than for the more viscous carbopol solution. In fact it can be estimated that the axial circulation flow is about twice as fast for the water. This is because after 3.75 s, the higher conductivity from the pulse

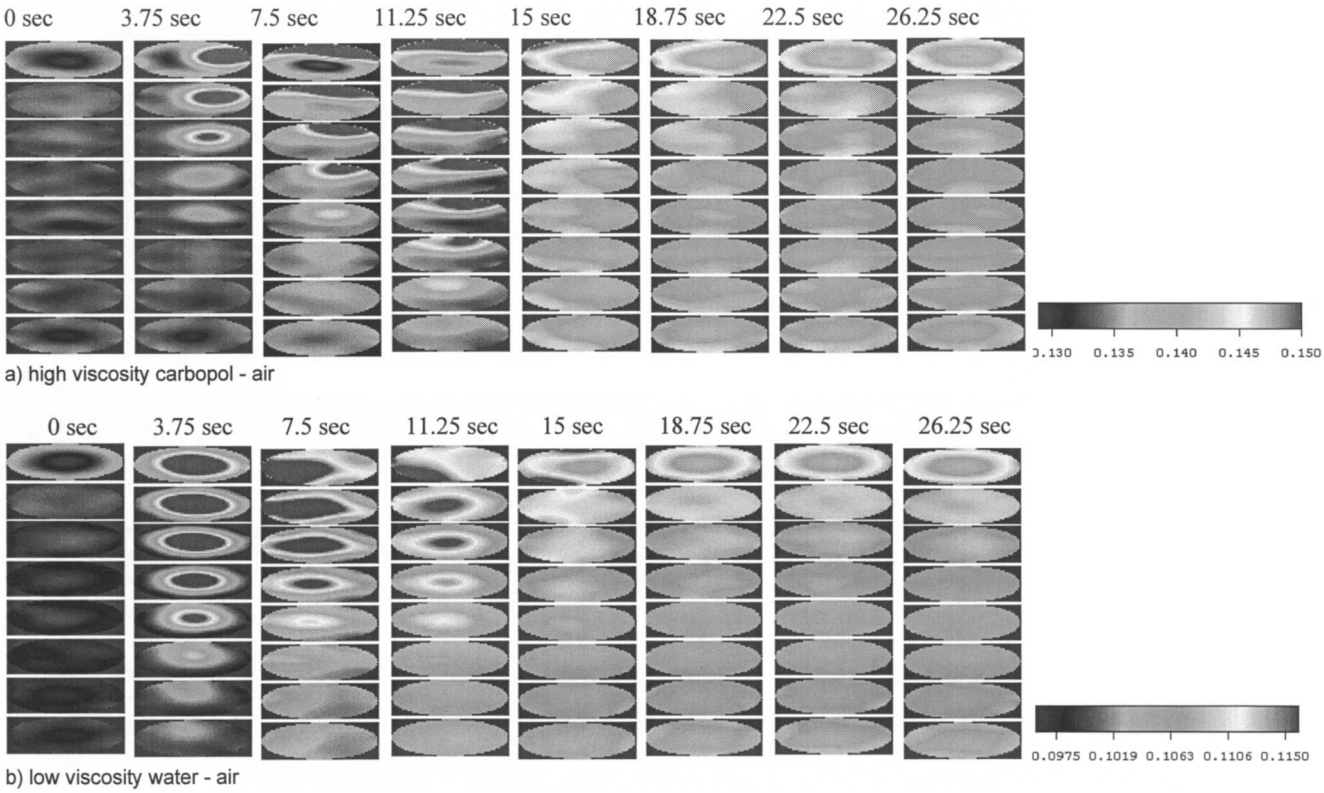

Fig. 3. Tomograms of liquid phase mixing of a brine tracer pulse.

has only just reached the mid-point whereas for water it has reached the lowest plane adjacent to the vessel base. This pattern of faster mixing for water is confirmed in the next two 'frames' at 7.5 and 11.25 s.

Fig. 3a and b also indicate that the tangential swirling flow is greater for the water, Thus, in the second set of tomograms, at 3.75 s, the regions of higher conductivity are more symmetrical then for the more viscous carbopol. A faster tangential flow will also promote faster mixing of a point injected tracer, which is borne out by the subsequent faster approach to the final uniform condition. The lack of total uniformity in the top tomograms in the final 'frames' is thought to be an artefact of the contour colour-filling which highlights an unevenness in gas hold-up close to the top-most sensing plane. This is probably caused by occasional repetitive surface disturbances due to randomly precessing vortices which intermittently suck bubbles into the body of upper fluid. These bubbles tend to be also randomly and irregularly re-released to the surface as these vortices individually and unpredictably subside.

4.2. Temporal mixing curves

It has already been demonstrated that electrical tomography can be used to construct mixing curves for any pixel in any of the eight sensing planes fitted to the 1.5 m vessel [2]. Examples of this interchangeability of spatial and temporal representation are shown in Fig. 4. This figure depicts two sets of mixing curves (corresponding to the top and bottom planes) derived from the air–water (low viscosity) and air–carbopol (high viscosity) results already displayed in Fig. 3.

For each experiment, the peripheral tomographic measurements are reconstructed (by linear back projection) onto a 76×76 matrix of pixels, with each axis (in the plane) marked from -38 to $+38$ so that the co-ordinate origin is at the centre of the vessel. The pulse injection pixel corresponds to $(0, -19)$ at the liquid surface. The mixing curves in Fig. 4 then are for detection at pixels (0, 19) in plane I (the top most) and 8 (the lowest). These are diametrically

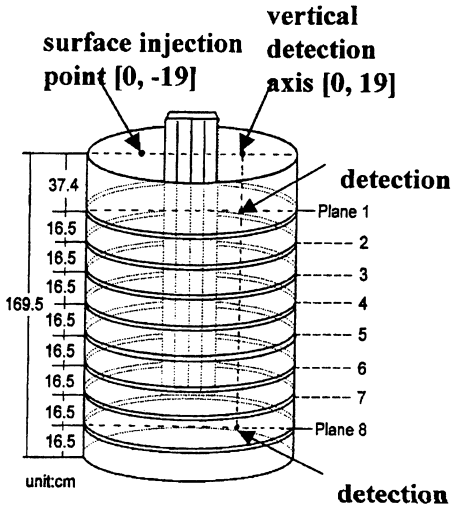

Fig. 5. Injection and detection pixels for mixing curves.

opposite to the injection pixel and similarly located midway between the vessel wall and impeller shaft. These coordinates for injection (of the pulse) and detection (of the mixing curve) are indicated in Fig. 5.

The real time mixing curves in Fig. 4 again confirm that the rate of mixing in water is much faster than in the viscous carbopol solution. For water, the top and base plane curves become equalised at $\approx$20 s indicating that the liquid phase has become close to homogenised. However, in contrast, even after 25 s the carbopol solution is not fully mixed. This value is close to a value of 26 s predicted by the Ruszkowski correlation [11]. Fig. 4 also demonstrates that there are distinct differences in the qualitative character of the liquid phase mixing in the low and high viscosity cases. For low viscosity water, there is a large overshoot on the path to final uniformity at the top of the vessel (plane 1), whereas there is no such overshoot at the lowest plane close to the vessel base. This indicates a relatively slower interchange rate between the liquid phase above and below the impeller. In contrast, air carbopol shows an intermediate attenuated behaviour. By comparison, there is a lower mixing

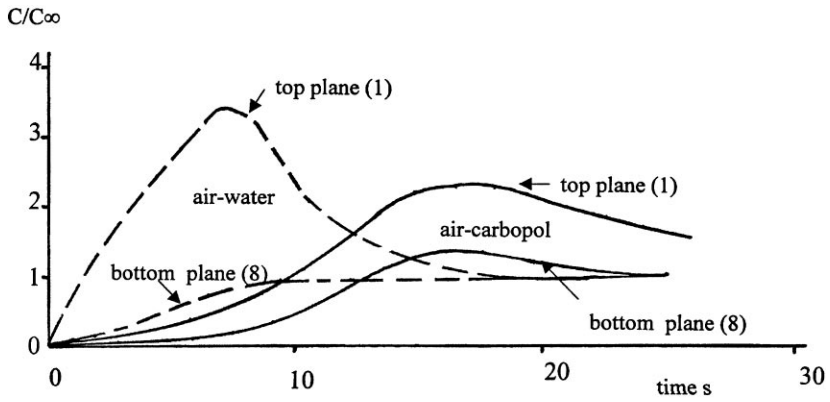

Fig. 4. Liquid phase mixing curves for gas–liquid mixing.

curve overshoot at the top of the vessel, but a larger relative overshoot (actually the comparitor mixing curve shows no maximum, but monotonically rises) at the bottom. Interestingly, the mixing curves for the high viscosity case thus show an apparently faster rate of relative mixing between the liquid phase above and below the impeller. These flow rate interchanges between fluid above and below the impeller somehow reflect the complexities of the fluid mechanics in 3-D.

The mixing curves in Fig. 4 are relatively very smooth because they are constructed from just a few pixel measures at 3.75 s intervals. They do not, therefore, exhibit the noise usually associated with much higher frequency acquisition. This is not expected to distort the general shape of the mixing curve responses and the actual local gas hold-up is not believed to affect them.

Both Figs. 3 and 4, by providing a high density of experimental information on the dynamic liquid phase mixing in 3-D, generate new and powerful means for resolving the fluid flow fundamentals in this complex two-phase gas–liquid mixing example either using CFD [3,4,7] or the simpler networks-of-zones [6].

5. Conclusions

For a 1.5 m plant-scale stirred vessel, an 8-plane 16-ring elements ERT system can detect and reconstruct the pseudo-stationary pattern of gas–liquid mixing in 3-D caused by local variations in dispersed gas hold-up (voidage). This system is sufficiently sensitive to measure differences in gas–liquid mixing which arise for fluids of different viscosity. Using solid-body graphics in 3-D, the differences between low viscosity water (1 cP) and a 0.05% carbopol solution (≈100 cP) can be readily visualised. Moreover, if the spatially variable gas hold-up effect is zeroed in each plane to provide a new set of baselines, the rates and pattern of liquid phase mixing can be isolated from the gas–liquid mixing by reconstructing the changes in resistivity as a pulse of high conductivity tracer is dynamically mixed throughout the fluid. The results, cast into stacks of 8-element tomograms, can readily visualise the faster rate of mixing in the low viscosity water at identical stirrer speeds and gas flows. Reconstructed tomograms for any plane can be interpreted to generate a temporal mixing curve for any nominated pixel in the plane. These results in 3-D will be useful for validating CFD models for gas–liquid mixing in stirred vessels [6,7].

Acknowledgements

The authors gratefully acknowledge support from EPSRC under the Foresight Programme GR/L37434 ‘Process Tomography: A New Dimension in Advanced Sensor Technology’.

References

[1] R. Mann, J. Dickin, M. Wang, T. Dyakowski, R.A. Williams, R.B. Edwards, A.E. Forrest, P.J. Holden, Application of electrical resistance tomography to interrogate mixing processes at plant scale, Chem. Eng. Sci. 52 (1997) 2087–2097.
[2] P.J. Holden, M. Wang, R. Mann, F.J. Dickin, R.B. Edwards, Imaging stirred vessel macromixing using electrical resistance tomography, A.I.Ch.E. JI. 44 (1998) 780–790.
[3] R.P. Zipp, G.K. Patterson, Experimental measurement and simulation of mixing and chemical reaction in a stirred tank, Can. JI. Chem. Eng. 76 (1998) 657–669.
[4] K. Ng, N.J. Fentiman, K.C. Lee, M. Yianneskis, Assessment of clicking mesh CFD predictions and LDA measurements of the flow in a tank stirred by a Rushton impeller, Trans. I. Chem. E. 76(A) (1998) 737–747.
[5] R.A. Williams, R. Mann, F.J. Dickin, O.M. Ilyas, P. Ying, R.B. Edwards, A. Rushton, Application of electrical impedance tomography to mixing in stirred vessels, A.I.Ch.E. Symp. Series 293 (1993) 8–15.
[6] R. Mann, R.A. Williams, T. Dyakowski, F.J. Dickin, R.B. Edwards, Development of mixing models using electrical resistance tomography, Chem. Eng. Sci. 52 (1997) 2073–2085.
[7] H.J. Warnecke, M. Schafer, J. Pruss, M. Weidenbach, A concept to simulate an industrial size tube reactor with fast complex kinetics and absorption of two gases on the basis of CFD modelling, Chem. Eng. Sci. 54 (1999) 2513–2519.
[8] P.J. Holden, M. Wang, R. Mann, F.J. Dickin, R.B. Edwards, On detecting mixing pathologies in a stirred vessel using electrical resistance tomography, Trans. I. Chem. E. (1999), submitted for publication.
[9] J. Bond, J.C. Cullivan, N. Climpson, I. Faulkes, X. Jia, J.A. Kostuch, D. Payton, M.Wang, S.J. Wang, R.M. West, R.A. Williams, Industrial monitoring of hydrocyclone operation using electrical resistance tomography, Chem. Eng. JI. (1999), this volume.
[10] D.S. Vlaev, M. Wang, T. Dyakowski, R. Mann, B.D. Grieve, Detecting filter cake pathologies in solid-liquid filtration: semi-tech scale demonstrations using electrical resistance tomography (ERT), Chem. Eng. JI. (1999), this volume.
[11] A.W. Nienow, On impeller circulation and mixing effectiveness in the turbulent flow regime, Chem. Eng. Sci. 52 (1997) 2557–2565.